Optics and Lasers in Engineering 196 (2026) 109392

Contents lists available at ScienceDirect

Optics and Lasers in Engineering

journal homepage: www.elsevier.com/locate/optlaseng

Laser scanning control and alignment method in 3D LDV

Zhengzhe Li [a,1], Zhipeng Zhang [a,1], Ruqiang Lai [a], Tao Zhang [b], Jian Li [a], Jinyu Ma [a], Xinjing Huang [a,*]

[a] State Key Laboratory of Precision Measurement Technology and Instruments, Tianjin University, Tianjin, China
[b] Tianjin Institute of Metrological Supervision and Testing, Tianjin, China

ARTICLE INFO

Keywords:
3D alignment
Laser attitude control
Laser doppler vibrometry

ABSTRACT

3D full-field scanning laser Doppler vibrometry (3D FFS LDV) offers significant advantages, including non-contact measurement, wide frequency bandwidth, and high accuracy, demonstrating considerable value in structural health monitoring, modal analysis, and ultrasonic testing applications. This paper investigates novel scanning and alignment control methodologies for 3D FFS LDV systems. First, the relationship between the control model of 2D rotating mirrors and the spatial vectors of laser beams is investigated. A laser beam attitude control algorithm is developed and implemented to estimate the laser spot positions, thereby achieving precise scanning control of the laser beam. Based on this foundation, a novel laser 3D alignment method based on singular value decomposition is proposed, which is a mathematical method that decomposes a matrix into simpler components to solve linear algebra problems. This method is designed to solve the transformation matrix between the probe and measurement coordinate systems, and this matrix can describe the spatial correlation between two distinct coordinate systems and enable coordinates conversion between them, enabling orthogonal measurement of vibration in the global coordinate system. Experimental validation demonstrates that the proposed method achieves laser scanning and control errors of 0.2 ~ 0.4 mm using fitting orders $m = 2$ and $n = 2$ with 8–9 non-concentrated calibration points. Practical testing verified that the 3D alignment accuracy on the pipe surface is within 4.71 %, while the simulation results verify that the 3D alignment accuracy on complex wavy surfaces is within 2.64 %, providing a reliable foundation for subsequent vibration velocity decomposition and modal analysis applications.

1. Introduction

Laser Doppler Vibrometer (LDV) is a non-contact instrument that measures vibration velocities on the surface of vibrating objects. This technology offers significant advantages, including no contact loading, high accuracy, and broad bandwidth, with applications spanning diverse fields such as modal testing and analysis, structural health monitoring, and ultrasonic flaw detection [1–3]. An LDV projects a laser beam onto a vibrating target surface, where the Doppler effect induces a frequency shift in the scattered light relative to the reference beam. The vibration velocity of the target is then obtained by detecting this frequency shift [4,5].

LDV systems can be classified into three categories: one-dimensional (1D), three-dimensional (3D), and three-dimensional full-field scanning (3D FFS) systems. 1D LDV is limited to measuring only the component of surface vibration along the laser beam direction [6–8]. When the angle between the laser beam and vibration direction becomes too large, the measured vibration amplitudes are significantly attenuated or may become undetectable. Furthermore, 1D LDV is inherently limited in its ability to fully characterize the 3D modal properties of an object. A 3D LDV can be configured by integrating three 1D LDVs with their laser beams converging at a single point, enabling simultaneous measurement of vibrations in three directions. Through coordinate transformation, the three non-orthogonal velocity measurements at a single point are decomposed and synthesized to achieve 3D vibration measurement within the global world coordinate system (WCS). When the measurement point changes, the orientation and position of all the three LDVs must be readjusted to ensure that the three laser beams converge at the new point. In contrast, 3D FFS LDV controls the two-axis deflection of three laser beams to make the beams traverse freely across the structural

* Corresponding author.
E-mail address: huangxinjing@tju.edu.cn (X. Huang).
[1] Zhengzhe Li and Zhipeng Zhang contributed equally to the work.

https://doi.org/10.1016/j.optlaseng.2025.109392
Received 19 May 2025; Received in revised form 28 September 2025; Accepted 3 October 2025
Available online 10 October 2025
0143-8166/© 2025 Elsevier Ltd. All rights are reserved, including those for text and data mining, AI training, and similar technologies.

surface while consistently converging at a single point. This eliminates the need to adjust the position and orientation of the three LDVs, thereby facilitating comprehensive 3D vibration measurements across the entire field.

Several research efforts have implemented 3D vibration measurements through sequentially positioning a single 1-D LDV at three different locations to illuminate the same measurement point. Dongkyu Kim conducted 3D vibration measurements by repositioning a single 1-D LDV and laser scanner at three distinct positions; although this approach offers cost advantages, it cannot synchronously acquire instantaneous 3D vibration velocities, thereby limiting its application scope [9,10]. Pierre Margerit mounted a 1D LDV on an industrial six-axis robotic arm and achieved target 3D velocity measurements by controlling the end-effector position and orientation, offering advantages of high flexibility and efficiency [11]. However, this method cannot simultaneously capture instantaneous 3D vibration velocities and introduces assembly errors associated with the robotic arm. Seppe Sels proposed a real-time estimation method for a single 1-D LDV's orientation and position based on matching camera images with CAD models, enabling real-time measurement of vibrations in any arbitrary direction on an object's surface; this method does not constitute true synchronous 3D velocity measurement and exhibits approximately 20 % greater error compared to conventional approaches using three tripod-mounted 1-D LDVs [12]. The aforementioned studies, which achieve 3D vibration measurements through translational or rotational positioning of a single 1-D LDV, demonstrate relatively low measurement efficiency and accuracy. These approaches cannot synchronously measure instantaneous 3D vibrations and are therefore applicable only to scenarios where vibration patterns remain stable or occur repeatedly.

3D LDV employs three 1-D LDVs to synchronously measure vibrations in three directions at a specific point on the measured object. Christian Rembe achieved picometer-level amplitude resolution by utilizing a main probe to emit a laser beam while three probes simultaneously received reflected light from the measured object [13]. However, due to the fixed relative positions of the three probes, the intersection point of the three laser beams remains stationary, thereby limiting the measurement range and preventing scanning-based measurements. Miyashita measured 3D vibrations using three 1-D LDVs and calculated the unit vectors of the three probe emission beams in the global WCS based on known grid point coordinates on a calibration plate. A transformation matrix from the three laser beam unit vectors to the global WCS was then constructed to facilitate 3D vibration measurements. When the measurement point changes, the orientation and position of all three LDVs require readjustment to ensure that the three laser beams converge at a single point [14]. Building upon the 3D LDV foundation, 3D FFS LDV controls the spatial position and direction of emission beams through three pairs of rotating mirrors to realize 3D FFS vibration measurements of large-scale objects. Zhu developed a Continuous Scanning Laser Doppler Vibrometer (CSLDV, a type of 3D FFS LDV) that employs an external controller to synchronize the movement of three LDV laser beams, facilitating scanning-based measurements of 3D vibrations [15–19]. Nevertheless, this approach requires a calibration plate to determine the transformation matrix from the three beam unit vectors to the global coordinate system. In summary, 3D FFS LDV demonstrates the most significant advantages; however, precise control of the three pairs of rotating mirrors and accurate beam vector coordinate transformation remain critical challenges.

Both directionally fixed 3D LDV and variable beam direction 3D FFS LDV systems share a fundamental limitation: each vibrometry probe can only measure vibration velocity along its own emitted laser beam direction in the local probe coordinate system (PCS), with the three laser beams being non-orthogonal to each other. To obtain 3D vibration components in the global WCS, the vibration velocities measured along three non-orthogonal directions in the PCS must be transformed into three velocity components in the global WCS. This transformation necessitates the calculation of unit vectors for each probe's emitted laser beam within the global WCS. The spatial directions of laser beams emitted by the three LDVs are known within their respective PCSes; therefore, the key to achieving 3D vibration measurements lies in obtaining the transformation matrices from the local PCSes to the global WCS. Specifically, this method is designed to solve the transformation matrix between the local PCSes and the global WCS — this matrix can describe the spatial correlation between these two distinct coordinate systems, enable coordinate conversion between them, and further support orthogonal measurement of vibration in the global coordinate system. The measured laser-direction velocities from each probe are transformed into 3D vibration components in the global coordinate system using the derived rotation matrices.

To address coordinate transformation issues in 3D alignment, various researchers have proposed diverse calibration methods and improvement strategies. However, limitations in these approaches provide critical directions for improvement in the present study. Zeng employed the least squares method with four or more alignment points to determine the directional transformation matrix [20]. However, this approach is significantly influenced by initial iterative values during the iteration process and requires a relatively accurate initial estimate. The method potentially yields two transformation matrices with opposite signs, necessitating further identification of the correct transformation matrix. Martarelli extended Zeng's calibration method by utilizing a theodolite to obtain world coordinates of calibration points. They investigated uncertainty sources from both theoretical and experimental perspectives and analyzed how the quantity and distribution of alignment points affect calibration accuracy [21]. Xu and Miles formulated an inverse method for determining transformation matrices by utilizing four reference points with known world and probe coordinates. The transformation matrix was obtained through the multiplication of the world coordinate matrix and the inverse of the probe coordinate matrix [22]. However, this method does not guarantee that the resulting matrix is orthogonal, which is inconsistent with physical reality and potentially introduces certain errors. Furthermore, the four reference points employed in this method must be distributed across different planes, making it suitable only for curved surfaces or other complex structures. To address these limitations, Chen improved upon the aforementioned methods by implementing singular value decomposition. Their approach calculates LDV's position and orientation using four or more target points with known coordinates, ensuring orthogonal transformation matrices applicable to arbitrary structures and enabling accurate determination of 3D velocity vectors [15]. However, this method requires a calibration board to achieve satisfactory accuracy.

This paper designs and implements an integrated hardware-software system for 3D alignment and scanning control for 3D FFS LDV. A geometric model for the emitted beam of two-axis cascaded rotating mirrors is established, yielding the mathematical relationship between emission vectors and rotation angles of two-dimensional rotating mirrors. A polynomial fitting-based method for laser scanning calibration and control is subsequently proposed. Precise control of the probe's laser beam incident position is achieved by manipulating the angles of two rotating mirrors, enabling high-precision 3D scanning control across multiple laser grid points. A 3D alignment algorithm based on singular value decomposition is proposed and validated for determining the rotation matrices between individual PCSes and the global WCS. Experimental results demonstrate that the algorithm exhibits excellent applicability and alignment precision. The proposed method offers advantages of low computational complexity and high accuracy, ensuring strictly orthogonal transformation matrices that provide a foundation for subsequent applications of 3D vibration's orthogonal decomposition in the WCS.

2. Principles of scanning and alignment

The designed 3D scanning laser control system is illustrated in Fig. 1. This system comprises three structurally identical laser scanning probes,

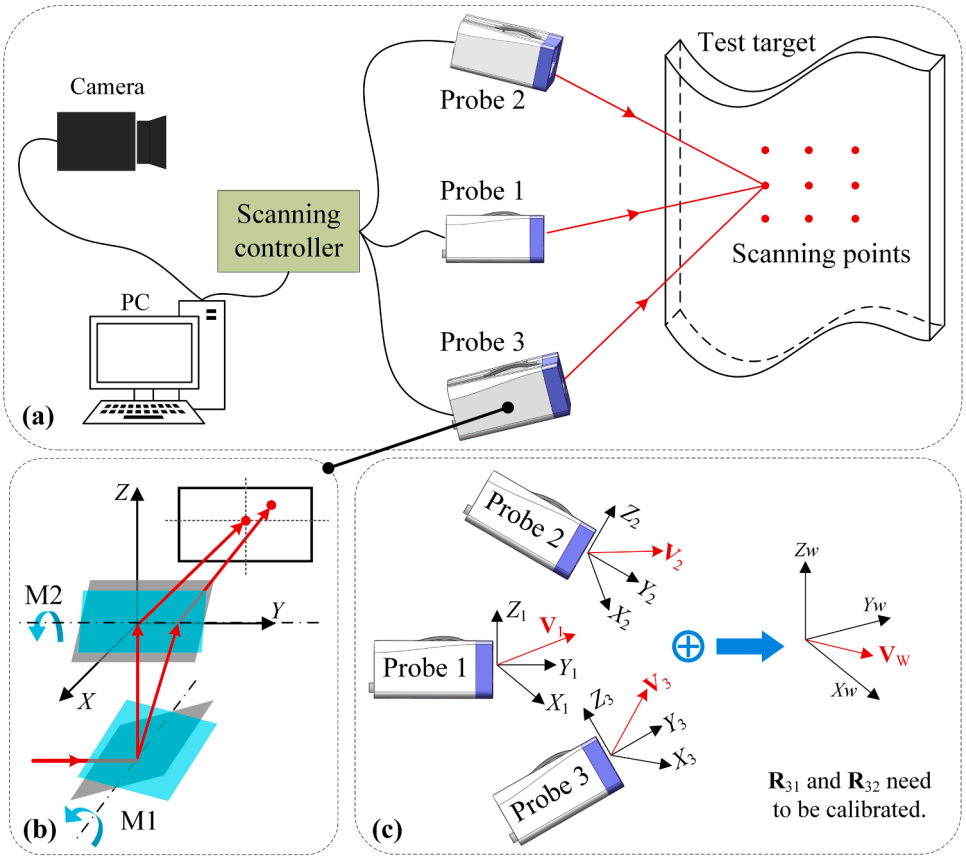

Fig. 1. System block diagram. (a) Front-end scanning control system. (b) Two-axis rotating mirror. (c) 3D alignment method.

a front-end scanning control system, and a camera. Each probe incorporates a laser rangefinder and a pair of two-axis rotating mirrors with fixed relative positions, enabling both spatial angle control of the emitted beam and precise distance measurement of the laser spot. The mathematical model for the rotating mirrors and laser spot position is established in Section 2.1. Based on this foundation, a polynomial fitting-based algorithm for controlling the spatial angle of laser beams is developed in this study. This algorithm achieves precise control of laser spots within the calibration region by fitting polynomial coefficients between the screen pixel coordinates of laser spot centers and the corresponding two mirror rotation angles. Detailed principles are presented in Section 2.2. To decompose and synthesize the measured non-orthogonal vibration velocities along the laser beam directions in the PCSes into the global WCS, a 3D alignment algorithm based on singular value decomposition is proposed. The algorithm unifies the coordinate systems of the three vibrometry probes by calculating the rotation and translation matrices between probe 1 and probe 2, as well as between probe 1 and probe 3. This establishes a foundation for subsequent applications such as vibration velocity's 3D orthogonal decomposition and modal analysis. The specific 3D alignment principle is described in Section 2.3.

2.1. *Mathematical model of two-axis rotating mirrors*

Each laser probe consists of a pair of rotating mirrors and a laser rangefinder. Rotating mirrors M1 and M2 are driven by separate motors,

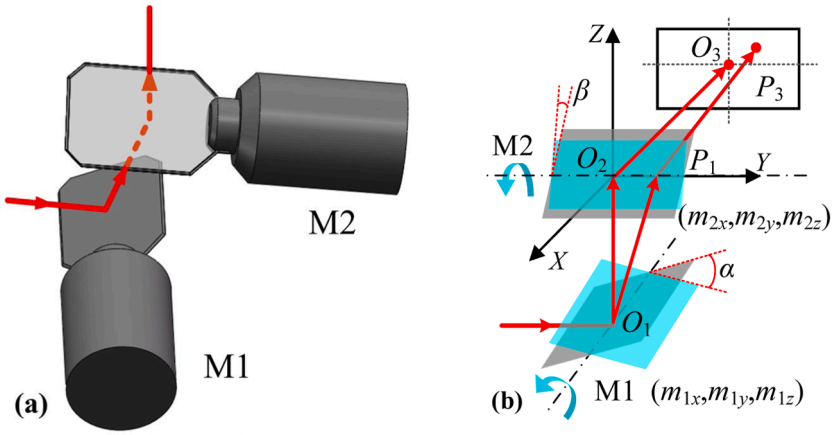

Fig. 2. Laser rotation control method via two mirrors. (a) Rotating mirror's geometric mode. (b) l two-axis mirror's rotation mod el.

with their angular positions maintaining a linear correspondence to the applied motor voltages. As illustrated in Fig. 2, a right-handed Cartesian PCS O_2-XYZ is established with the center O_2 of mirror M2 as the origin, where the Y-axis is the rotation axis of mirror M2. The rotation axis positions and initial angles of mirrors M1 and M2 are fixed during manufacturing. The rotation angles of mirrors M1 and M2 are denoted as α and β, respectively. When $\alpha = \beta = 0$, the laser beam passes sequentially through the centers of M1 and M2. Within the O_2-XYZ coordinate system, the unit spatial vector of the laser beam emitted from the laser source is denoted as $\mathbf{S} = (0,1,0)^{\mathrm{T}}$. The unit vectors of the rotation axes for mirrors M1 and M2 are designated as $\mathbf{m}_1 = (m_{1x}, m_{1y}, m_{1z})^{\mathrm{T}}$ and $\mathbf{m}_2 = (m_{2x}, m_{2y}, m_{3z})^{\mathrm{T}}$, respectively. The initial normal vectors of M1 and M2 when $\alpha = 0$ or $\beta = 0$ are represented by $\mathbf{n}_1 = (n_{1x}, n_{1y}, n_{1z})^{\mathrm{T}}$ and $\mathbf{n}_2 = (n_{2x}, n_{2y}, n_{2z})^{\mathrm{T}}$.

Using the unit vector $\mathbf{m}_1$ of M1's rotation axis, the rotation matrix $\mathbf{R}_1$ for the normal vector of M1 can be constructed as follows [23]:

$$\mathbf{R}_1 = e^{\hat{\gamma}_1 \alpha} = \mathbf{I} + \hat{\gamma}_1 \sin\alpha + \hat{\gamma}_1{}^2(1 - \cos\alpha) \tag{1}$$

where $\mathbf{I}$ represents the identity matrix,

$$\hat{\gamma}_1 = \begin{pmatrix} 0 & -m_{1z} & m_{1y} \\ m_{1z} & 0 & -m_{1x} \\ -m_{1y} & m_{1x} & 0 \end{pmatrix} \tag{2}$$

The reflection matrix $\mathbf{M}_1$ for the laser beam by mirror M1 is expressed as:

$$\mathbf{M}_1 = \left(\mathbf{I} - 2(\mathbf{R}_1\mathbf{n}_1)(\mathbf{R}_1\mathbf{n}_1)^{\mathrm{T}}\right) \tag{3}$$

In the O_2-XYZ coordinate system, the center point O_1 of mirror M1 is known, and the normal vector of M1 is $\mathbf{n}_{1\alpha} = \mathbf{R}_1\mathbf{n}_1$. Consequently, O_1 and $\mathbf{n}_{1\alpha}$ uniquely determine the linear equation of the laser beam $\overrightarrow{\mathbf{O_1P_2}}$ after reflection from M1. Similarly, the normal vector of M2 is $\mathbf{n}_{2\beta} = \mathbf{R}_2\mathbf{n}_2$, thus $O_2\ (0,0,0)^{\mathrm{T}}$ and $\mathbf{n}_{2\beta}$ uniquely determine the plane equation of M2. Therefore, the intersection point P_2 of $\overrightarrow{\mathbf{O_1P_2}}$ with M2 can be calculated, which represents the reflection point of the laser beam on M2.

The reflection matrix $\mathbf{M}_2$ for the laser beam by mirror M2 is expressed as:

$$\mathbf{M}_2 = \left(\mathbf{I} - 2(\mathbf{R}_2\mathbf{n}_2)(\mathbf{R}_2\mathbf{n}_2)^{\mathrm{T}}\right) \tag{4}$$

Therefore, the unit vector $\overrightarrow{\mathbf{P_2P_3}}$ of the laser beam after reflection from mirrors M1 and M2 is given by:

$$\mathbf{O}_L = \mathbf{M}_2\mathbf{M}_1\mathbf{S} \tag{5}$$

The spatial coordinates of P_3 of the laser spot on the measured object can be determined using the coordinates of the intersection point P_2, the emitted laser beam unit vector $\mathbf{O}_L$, and the distance L between the emission point and the measured object, through the equation $\overrightarrow{\mathbf{O_2P_3}} = \overrightarrow{\mathbf{O_2P_2}} + L{\cdot}\mathbf{O}_L$.

In the 2D rotating mirror system designed in this study, within the O_2-XYZ coordinate system, the unit vectors of the rotation axes for M1 and M2 are $\mathbf{m}_1 = (1,0,0)^{\mathrm{T}}$ and $\mathbf{m}_2 = (0,1,0)^{\mathrm{T}}$, respectively, while the coordinates of the M1 center O_1 are $(0,0,-d)$. When $\alpha = \beta = 0$, mirrors M1 and M2 are at their initial angles, with M1 forming a 45° angle with the XOZ plane and M2 forming a 45° angle with the YOZ plane. The initial normal vectors of M1 and M2 are $\mathbf{n}_1 = \left(0, -\sqrt{2}/2, \sqrt{2}/2\right)^{\mathrm{T}}$ and $\mathbf{n}_2 = \left(-\sqrt{2}/2, 0, -\sqrt{2}/2\right)^{\mathrm{T}}$, respectively. The spatial vector of the laser beam on the measured object is ultimately derived as:

$$\overrightarrow{\mathbf{O_2P_3}} = \overrightarrow{\mathbf{O_2P_2}} + L{\cdot}\mathbf{O}_L = \begin{pmatrix} -L\cos(2\beta) \\ L\sin(2\alpha) - d{\cdot}\tan(2\alpha) \\ -L\cos(2\alpha)\sin(2\beta) \end{pmatrix} \tag{6}$$

where L represents the distance measured by the laser rangefinder from the emission point on rotating mirror M2 to the incident point on the measured object.

2.2. Laser beam control algorithm

As indicated by Eq. (6), the coordinates of the laser spot on the measured object are uniquely determined by the distance and deflection angles of the rotating mirrors. To precisely control the position of the laser spot on the measured object surface and achieve automated scanning, a camera is employed to map the three-dimensional spatial coordinates of the laser spot to a screen pixel coordinate system, thereby monitoring the convergence of laser spots from the three probes. As illustrated in Fig. 3, several calibration points are selected on the surface of the measured object. The pixel coordinates (x_i, y_i) corresponding to each marked point P_i are recorded, along with the deflection angles (α_i, β_i) of the rotating mirrors when the laser spot is positioned at point P_i. A mapping relationship between the rotation angles of the mirrors and the corresponding laser pixel coordinates at these calibration points is established and used to realize precise movement of the laser to arbitrary positions on the measured object. This process constitutes a fundamental and essential step for PCS alignment of the three probes and co-point scanning control of the laser beams.

According to Eq. (6), the coordinates of the measured object in the PCS can be determined using the rotation angles of the mirrors. In conjunction with the camera's pixel coordinate system, a 2D polynomial function is employed to fit the mathematical relationship between the mirror rotation angles and the corresponding pixel coordinates of the calibration points. This relationship enables control of the three laser beams to consistently converge at the same point and perform precise scanning across the calibrated region. The fitting function is presented as:

$$\begin{cases} \alpha_i = \sum_{j=0}^{m}\sum_{k=0}^{n} A_{jk} x_i^j y_y^k \\ \beta_i = \sum_{j=0}^{m}\sum_{k=0}^{n} B_{jk} x_i^j y_y^k \end{cases} \tag{7}$$

Assuming i calibration points are selected to solve for the polynomial coefficient matrices $\boldsymbol{A}$ and $\boldsymbol{B}$ that establish the relationship between deflection angles α and β of rotating mirrors M1 and M2 at the calibration points and their corresponding pixel coordinates in the screen coordinate system. The calculation formulas are presented as follows:

$$\begin{bmatrix} A_{00} \\ A_{01} \\ A_{10} \\ \vdots \\ A_{mn} \end{bmatrix} = \begin{bmatrix} 1 & x_1^1 & y_1^1 & \cdots & x_1^m y_1^n \\ 1 & x_2^1 & y_2^1 & \cdots & x_2^m y_2^n \\ 1 & x_3^1 & y_3^1 & \cdots & x_3^m y_3^n \\ \vdots & \vdots & \vdots & \vdots & \vdots \\ 1 & x_i^1 & y_i^1 & \cdots & x_i^m y_i^n \end{bmatrix}^{+} \begin{bmatrix} \alpha_1 \\ \alpha_2 \\ \alpha_3 \\ \vdots \\ \alpha_i \end{bmatrix} \tag{8}$$

$$\begin{bmatrix} B_{00} \\ B_{01} \\ B_{10} \\ \vdots \\ B_{mn} \end{bmatrix} = \begin{bmatrix} 1 & x_1^1 & y_1^1 & \cdots & x_1^m y_1^n \\ 1 & x_2^1 & y_2^1 & \cdots & x_2^m y_2^n \\ 1 & x_3^1 & y_3^1 & \cdots & x_3^m y_3^n \\ \vdots & \vdots & \vdots & \vdots & \vdots \\ 1 & x_i^1 & y_i^1 & \cdots & x_i^m y_i^n \end{bmatrix}^{+} \begin{bmatrix} \beta_1 \\ \beta_2 \\ \beta_3 \\ \vdots \\ \beta_i \end{bmatrix} \tag{9}$$

The coordinate matrix in the above equation is typically non-square, therefore its pseudoinverse must be computed to solve for the coefficient matrix.

After obtaining the polynomial coefficient matrices $\boldsymbol{A}$ and $\boldsymbol{B}$ within the calibration region, the pixel coordinates on the screen can be substituted into Eq. (7) to determine the corresponding rotation angles α

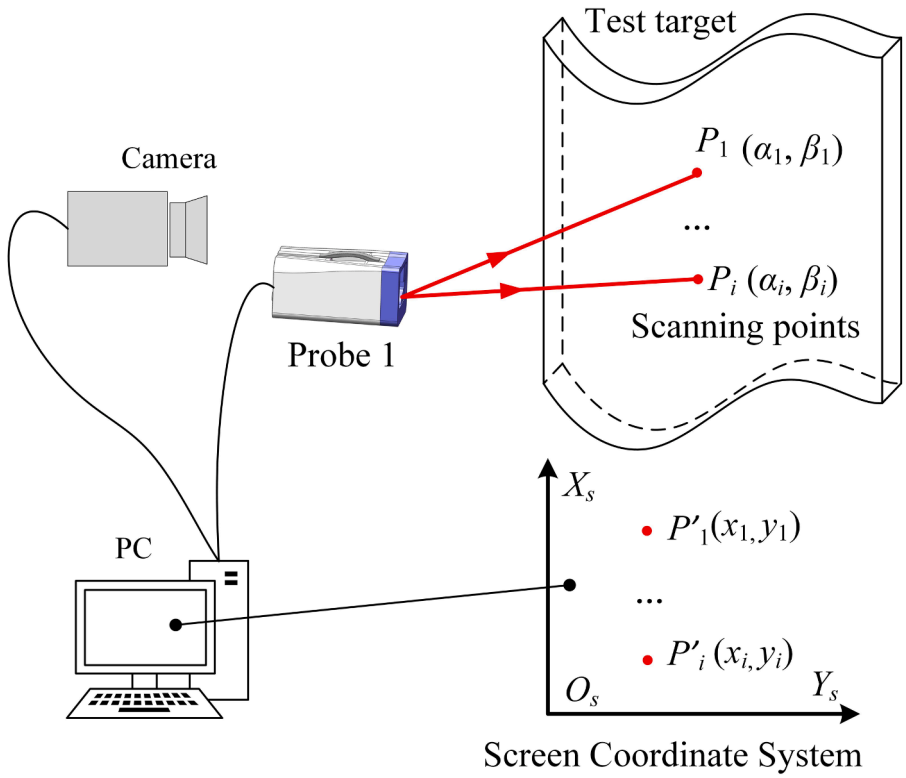

Fig. 3. Laser beam control via rotating mirror and camera feedback.

and β of the mirrors to achieve precise control over the laser spot position.

2.3. 3D alignment algorithm

The WCS serves as the foundation for 3D alignment algorithms. This paper establishes the WCS directly on one of the three probes. According to the mathematical model derived in Section 2.1, when the WCS is established based on the PCS, the coordinates of the laser spot in WCS can be calculated given the known rotation angles of the probe's rotating mirrors and the distance to the laser spot. During the calibration process for this probe, the mapping between the WCS and the pixel coordinate system is simultaneously calibrated using Eqs. (7)-(9) in Section 2.2. It means this calibration process inherently includes the calibration of the camera's intrinsic parameters.

Any local PCS can be designated as the global WCS. In this study, the PCS of probe 1 is selected to serve as the reference WCS. Assuming the vibration velocity magnitudes measured in the local PCSes of probes 1, 2, and 3 are V_1, V_2, and V_3 respectively, the three vector components of the measured vibration velocity can be calculated using Eq. (6) in the probe coordinate system. Taking $\mathbf{V}_1$ as an example, it can be calculated as follows:

$$\mathbf{V}_1 = V_1 \boldsymbol{e}_1 \tag{10}$$

where $\boldsymbol{e}$ denotes the unit direction vector of the laser beam emitted by the probe in the PCS.The resultant 3D vibration velocity vector $\mathbf{V}$ in the WCS is obtained using Eq. (11):

$$\mathbf{V} = \begin{bmatrix} \mathbf{e}_1{}^{\mathrm{T}} \\ \mathbf{R}_{12}\mathbf{e}_2{}^{\mathrm{T}} \\ \mathbf{R}_{13}\mathbf{e}_3{}^{\mathrm{T}} \end{bmatrix}^{-1} \cdot \begin{bmatrix} V_1 \\ V_2 \\ V_3 \end{bmatrix} \tag{11}$$

where $\mathbf{R}_{12}$ and $\mathbf{R}_{13}$ represent the rotation matrices between the WCS and the PCSes of probes 2 and 3, respectively. Therefore, the key to achieving 3D velocity measurement lies in determining the rotation matrices between the world coordinate system and the probe coordinate systems.

In the 3D alignment algorithm, several points can be selected in both the WCS and the PCS. By substituting the distances measured by the laser rangefinder and the probe rotation angles into Eq. (6), the coordinates in both coordinate systems can be obtained, forming two point sets $\{\mathbf{p}_i : i = 1, 2, \cdots, n\}$ and $\{\mathbf{p}'_i : i = 1, 2, \cdots, n\}$. The following relationship exists between these two point sets [24]:

$$\begin{bmatrix} x'_i \\ y'_i \\ z'_i \end{bmatrix} = \mathbf{T} + \mathbf{R} \begin{bmatrix} x_i \\ y_i \\ z_i \end{bmatrix} + \mathbf{N}_\mathbf{i} \tag{12}$$

where $[x_i \quad y_i \quad z_i]^{\mathrm{T}}$ and $[x'_i \quad y'_i \quad z'_i]^{\mathrm{T}}$ represent the coordinate vectors of point $\mathbf{p}_\mathbf{i}$ in the global WCS and point $\mathbf{p}'_\mathbf{i}$ in the local PCS, respectively, and $\mathbf{N}_\mathbf{i}$ denotes the noise matrix. The rotation matrix $\mathbf{R}$ is determined by minimizing the noise vector $\mathbf{N}_\mathbf{i}$, which can be formulated as:

$$\min\ (\mathrm{F}(\mathbf{R})) = \min\left(\sum_{i=1}^{n} \|\mathbf{p}'_\mathbf{i} - (\mathbf{R}\mathbf{p}_\mathbf{i} + \mathbf{T})\|^2 \right) \tag{13}$$

Defining $\overline{\mathbf{p}'} = \frac{1}{N}\sum_{i=1}^{N} \mathbf{p}'_\mathbf{i}$, $\overline{\mathbf{p}} = \frac{1}{N}\sum_{i=1}^{N} \mathbf{p}_\mathbf{i}$, $\mathbf{q}'_\mathbf{i} = \mathbf{p}'_\mathbf{i} - \overline{\mathbf{p}'}$ and $\mathbf{q}_\mathbf{i} = \mathbf{p}_\mathbf{i} - \overline{\mathbf{p}}$, then

$$\begin{aligned} \min(\mathrm{F}(\mathbf{R})) &= \min\left(\sum_{i=1}^{n} \|\mathbf{q}'_\mathbf{i} - \mathbf{R}\mathbf{q}_i\|^2 \right) \\ &= \min\left(\sum_{i=1}^{n} (\mathbf{q}_\mathbf{i}'^{\mathrm{T}}\mathbf{q}'_\mathbf{i} + \mathbf{q}_\mathbf{i}^{\mathrm{T}}\mathbf{q}_\mathbf{i} - 2\mathbf{q}_\mathbf{i}'^{\mathrm{T}}\mathbf{R}\mathbf{q}_\mathbf{i}) \right) \end{aligned} \tag{14}$$

Therefore, minimizing this expression is equivalent to maximizing the value of $\sum_{i=1}^{N} \mathbf{q}_\mathbf{i}'^{\mathrm{T}}\mathbf{R}\mathbf{q}_\mathbf{i}$, and this can be transformed into solving for the trace of the matrix as follows:

$$\max\left(\sum_{i=1}^{N}\mathbf{q_i}^{'\mathrm{T}}\mathbf{R}\mathbf{q_i}\right)=\max\left(\mathrm{Trace}\left(\sum_{i=1}^{N}\mathbf{R}\mathbf{q_i}\mathbf{q_i}^{'\mathrm{T}}\right)\right)=\max(\mathrm{Trace}(\mathbf{RH})) \tag{15}$$

where $\mathbf{H}=\sum_{i=1}^{N}\mathbf{q_i}\mathbf{q_i}^{'\mathrm{T}}$, this matrix can be decomposed using the singular value decomposition (SVD) method, which is a mathematical method that decomposes a matrix into simpler components to solve linear algebra problems. The decomposition is as follows:

$$\mathbf{H}=\mathbf{U}\Lambda\mathbf{V}^{\mathrm{T}} \tag{16}$$

where $\mathbf{U}$ and $\mathbf{V}$ are 3×3 orthogonal matrices, and Λ is a 3×3 diagonal matrix with non-negative elements.

When $\mathbf{R}=\mathbf{V}\mathbf{U}^{\mathrm{T}}$, the Trace($\mathbf{RH}$) reaches its maximum value [25], resulting in $\mathbf{p_i'}=\mathbf{R}\mathbf{p_i}+\mathbf{T}$, which indicates that the calculated matrix $\mathbf{R}$ represents the rotation matrix between the WCS and the PCS. Using the obtained rotation matrix $\mathbf{R}$ and Eq. (10), the 3D vibration velocity $\mathbf{V}$ in the WCS can be determined.

3. Scanning and alignment parameter testing

3.1. Experimental configuration and methodology

An experimental apparatus was constructed as illustrated in Fig. 4, comprising three structurally identical laser probes and a camera. Each laser probe consists of a laser rangefinder and a 2D rotating mirror system. A host personal computer (PC) serves as the master controller of the system, running customed software developed using the Qt framework. This software performs several key functions:

1. Controlling over the rotation angles of the 2D rotating mirrors M1 and M2.
2. Reading the distance measurements from the laser rangefinder.
3. Capturing the laser spot positions on the test structure in real-time via the camera.
4. Solving the rotation matrix and decomposing the vibration velocity vector.

The parameters of the camera and the laser rangefinder are shown in Table 1.

Table 1
Hardware parameter summary.

Hardware	Parameter	Specification
Camera	Pixel	2.3 million
	Pixel size	4.8 × 4.8 μm
	Resolution	1920 × 1200 pixels
	Frame rate	164 fps
Lens	Focal length	25 mm
Laser rangefinder	Laser type	Photo diode
	Laser wavelength	660 nm
	Measurement range	0.05 ~ 30 m
	Ranging accuracy	1 mm
	Measurement frequency	0 ~ 30 Hz
2D rotating mirrors	Reflectivity	99 %
	Scanning speed	25 Kpps
	Control accuracy	8 μRad

A pipe was selected as the test object. Various parameters affecting the performance of the laser beam direction control algorithm were tested, including fitting order, number of calibration points, and calibration point distribution. Tests were conducted on the number and distribution of calibration points for the 3D alignment algorithm to investigate their effects on the accuracy of the proposed algorithm.

3.2. Laser scanning control parameter testing

3.2.1. Polynomial fitting order testing

The distance r between the probe containing the rotating mirrors and the test structure was fixed at approximately 300 mm. Comparative experiments were conducted using different fitting orders (m, n) in (7), specifically (1, 1), (2, 1), (2, 2), (2, 3), (3, 2), (3, 3), (3, 4), (4, 3), and (4, 4). To facilitate comparison and eliminate other influencing factors, 8 calibration points were used, distributed approximately uniformly within a rectangular region. The distribution of calibration and validation points is illustrated in Fig. 5.

The rotation angles of the two mirrors were adjusted to direct the laser beam to different calibration points, and the corresponding angles and pixel coordinates were recorded. The polynomial coefficients were calculated using Eqs. (8) and (9), thereby completing the calibration.

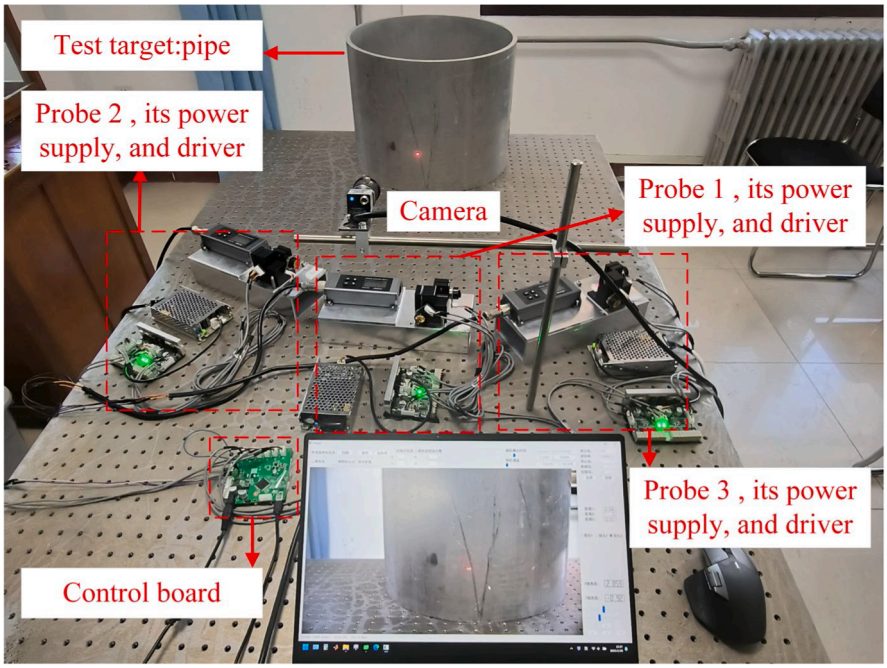

Fig. 4. Experimental apparatus.

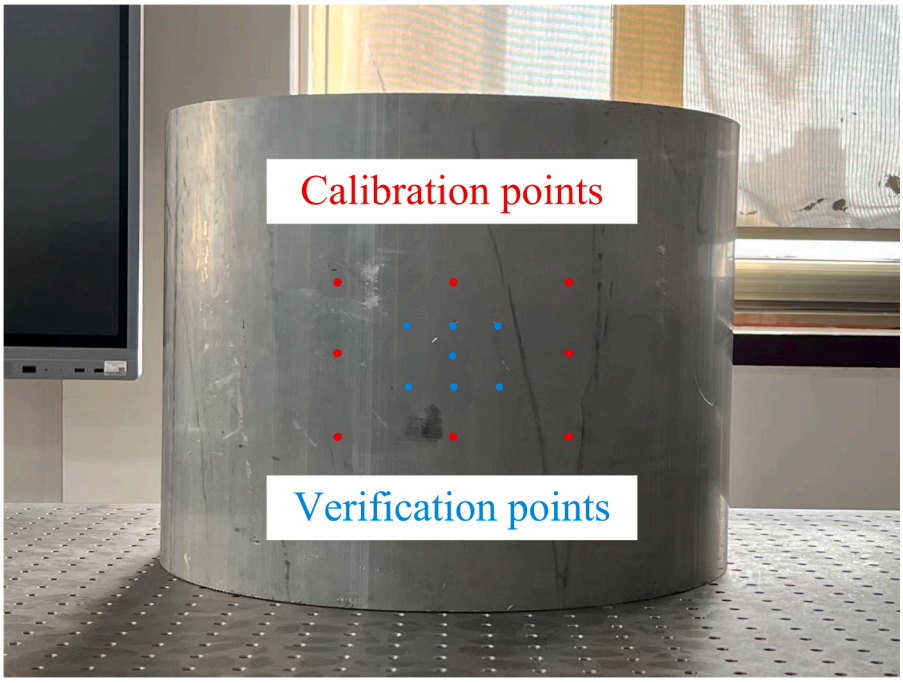

Fig. 5. Fitting order test experiment.

After calibration, the laser spot was moved to validation points with known mirror rotating angles. The rotation angles of both mirror axes corresponding to these points were then calculated from the pixel coordinates using Eq. (7). Subsequently, the calculated rotation angles were compared with the known actual angles of these points to determine the angular control error. Finally, the displacement control error at each point was calculated by multiplying the distance between the validation point and the rotating mirrors by the sine of the angular error. To minimize the influence of outliers, the root mean square error (RMSE) was calculated across all validation points to quantify the average error. This RMSE was used as the error evaluation parameter for experiments testing different fitting orders, numbers of calibration points, and calibration point distributions. The specific calculation method is given in Eq. (17):

$$\begin{cases} R_{M1} = r \times \sqrt{\sum_{i=1}^{N} (\alpha_i - \alpha_{it})^2 \Big/ N} \\ R_{M2} = r \times \sqrt{\sum_{i=1}^{N} (\beta_i - \beta_{it})^2 \Big/ N} \end{cases} \tag{17}$$

where R_{M1}, R_{M2} represent the root mean square error values the distance deviation of the laser spot in two directions, r = 300 mm, N is the number of validation points, α_i and β_i are the measured angles of the two mirror axes when reaching the specified validation points, while α_{it} and β_{it} denote the actual angles corresponding to these validation points.

7 fixed validation points within the calibration region were selected for error analysis, with the final error testing results illustrated in Fig. 6.

As demonstrated by the experimental results, the average positioning error for both mirror axes at the validation points achieves its minimum value when employing a polynomial fitting order of (2, 2) within the

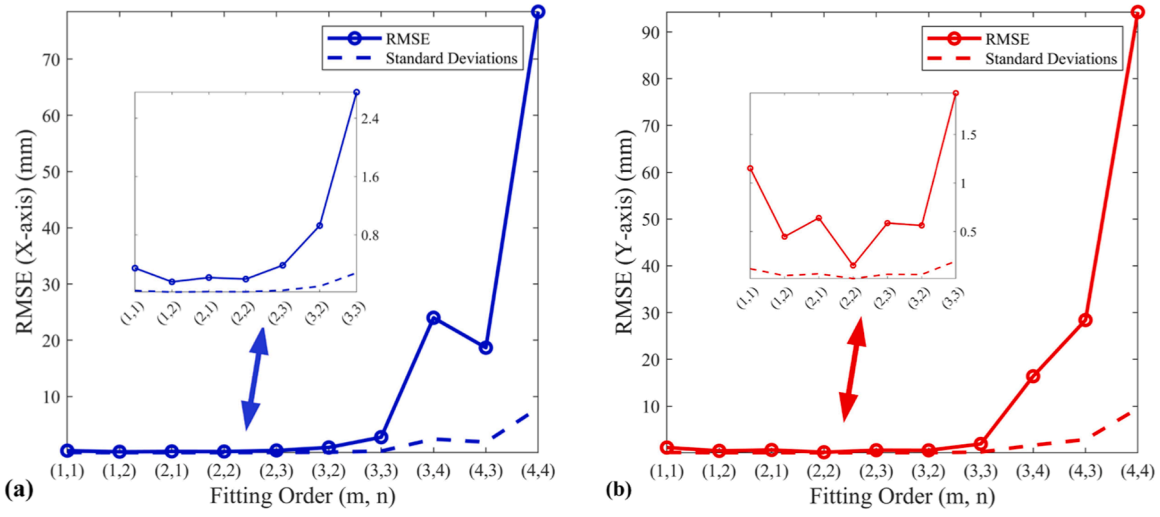

Fig. 6. Fitting order test results. (a) X-axis errors. (b) Y-axis errors.

calibrated measurement region. When the fitting order is too low, the fitting model cannot adequately capture the nonlinear relationship between the laser spot positions and mirror rotating angles, resulting in insufficient control precision. Conversely, when the fitting order is excessively high, the model complexity increases, which tends to cause overfitting and consequently leads to large control errors.

3.2.2. Calibration point number testing

To verify the effect of calibration point quantity on the precision of the laser spot control algorithm, experiments were conducted with 12 different sets of calibration points while maintaining a constant calibration region size. The number of validation points was maintained at seven with fixed positions, thereby ensuring the comparability of experimental results. The error calculation formula is shown in Eq. (17), with the root mean square error of validation points adopted as the evaluation metric. Through error analysis under different calibration point quantities, the relationship curve between the number of calibration points and error was obtained, as illustrated in Fig. 7.

The experimental results clearly demonstrate a significant negative correlation between the number of calibration points and measurement error. As the number of calibration points increases, the RMSE exhibits a pronounced downward trend. Specifically, when the number of calibration points increases from 2 to 8, the error drops dramatically from approximately 38 mm to <1 mm, indicating that increasing the number of calibration points during this phase significantly can enhance algorithm precision. However, when the number of calibration points exceeds 8, the error curve stabilizes, with values maintaining around 0.4 mm, suggesting that further increases in calibration points yield diminishing marginal returns in precision improvement, and the algorithm performance approaches saturation. Based on these experimental results, it can be concluded that in practical applications, the number of calibration points should be reasonably selected according to precision requirements and computational resource constraints. Under general circumstances, 8 calibration points are sufficient to meet basic precision requirements. Therefore, in practical applications, 8 or 9 calibration points are preferentially selected to ensure high precision while avoiding excessive computational resource consumption.

3.2.3. Calibration points distribution testing

To investigate the influence of calibration point distribution on the precision of the attitude control algorithm, two experimental configurations were implemented: 8 calibration points approximately uniformly distributed around the validation points within the calibration area of the image captured by the camera, and 8 calibration points distributed away from the validation points within the calibration area of the image, as illustrated in Fig. 8(a) and 8(b), respectively. The error calculation methodology adopts the RMSE as Eq. (17) of validation points as the evaluation criterion.

The test results are presented in Table 2. The results demonstrate that when the distribution area of calibration points fails to cover the region containing validation points, measurement errors increase significantly. In contrast, when validation points are located within the calibration region, errors are substantially lower. It is therefore evident that in practical 3D topography measurements, when the measured object has a relatively large volume, a method of uniformly distributed calibration points should be adopted to enhance measurement precision.

3.3. 3D alignment algorithm performance testing

When conducting the 3D alignment performance testing, the probe 1 was fixed, with the PCS 1 serving as the WCS, while the other two probes were rotated around the Z-axis by arbitrary known angles relative to the probe 1. Subsequently, the method proposed in this paper was employed to determine the rotation matrices between the PCS 2 and the WCS, and between the PCS 3 and the WCS. The vector error integration method was adopted to calculate the solution error of the rotation matrices. Assuming an arbitrary unit vector in space $\mathbf{n}' = (\sin\theta\cos\sigma, \sin\theta\sin\sigma, \cos\theta)$, where θ represents the angle between this vector and the Z-axis of the coordinate system with $\theta \in (0,\pi)$, and σ represents the angle between the projection of this vector on the XY plane and the X-axis with $\sigma \in (0, \pi)$. Both θ and σ vary from 0 to π. After fixing the positions of the three probes, rotation angles were measured using a high-precision angle gauge (repeatability error 0.05°), and the reference rotation matrices $\mathbf{R}_c$ between the probe 1 and the two other probes were obtained through coordinate system rotation transformation. During the measurement, the reference surface of the angle gauge was first brought into intimate contact with the mechanical datum surface of the probe 1 and zero-calibrated. It was then precisely rotated around its Z-axis until its measuring surface aligned with the datum surface of the probe 2 (or the probe 3), after which the reading from the angle gauge was recorded.

The unit vector $\mathbf{n}$' was multiplied separately by the calculated rotation matrix $\mathbf{R}$ and the reference rotation matrix $\mathbf{R}_c$, yielding the corresponding unit vectors $\mathbf{n}_{wc}$ and $\mathbf{n}_w$ in the WCS.

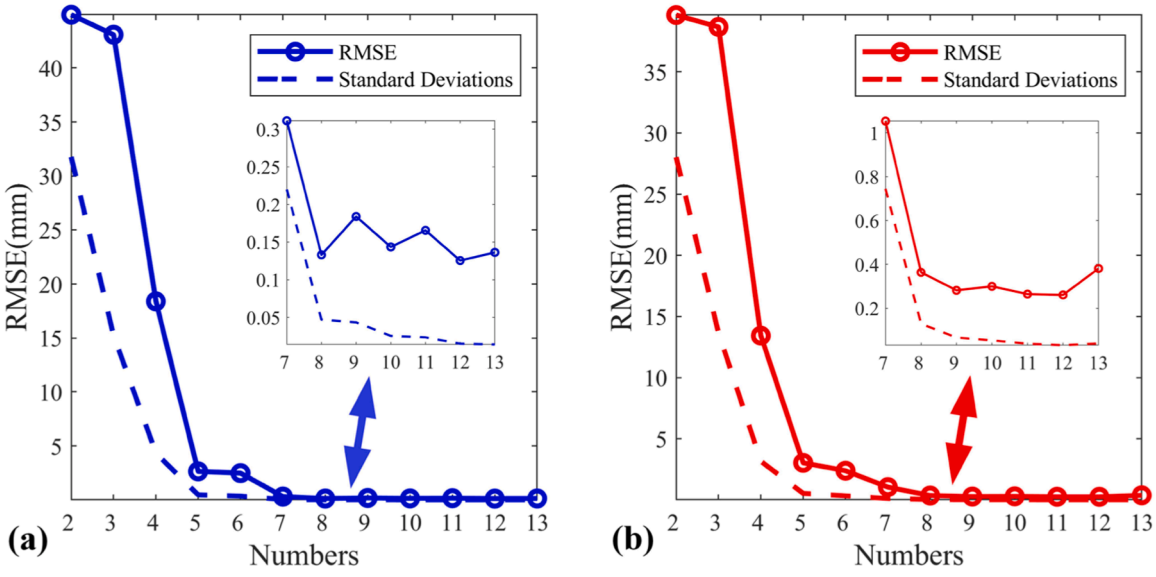

Fig. 7. Test results of the number of calibration points. (a) X-axis errors. (b) Y-axis errors.

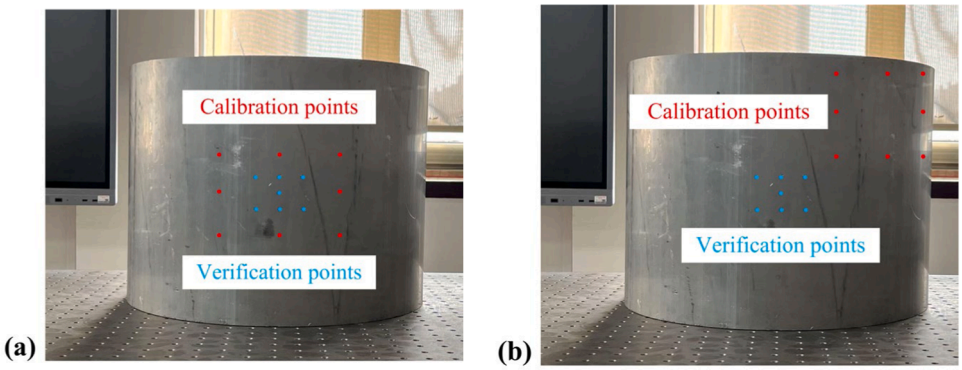

Fig. 8. Distribution of calibration points. (a) Calibration points surround measurement points. (b) Calibration points are away from measurement points.

Table 2
Test results of different distribution of calibration points.

Test Point	Error when calibration region surrounding measurement points		Error when calibration region is away from measurement points	
	Absolute error (mm)	RMSE (mm)	Absolute error (mm)	RMSE (mm)
1	(−0.05, 0.04)	(0.1,0.2)	(−2.9, −23.4)	(7.6,43.9)
2	(−0.01, −0.1)		(−0.6, −6.2)	
3	(−0.2, 0.4)		(0.3, −1.3)	
4	(0.2, 0.02)		(−4.4, −34.9)	
5	(0.04, −0.1)		(−9.4, −71.6)	
6	(0.08, −0.1)		(−0.1, −5.9)	
7	(−0.2, −0.1)		(−16.8, −80.8)	

$$\begin{cases} \mathbf{n}_{wc} = \mathbf{R}_c\mathbf{n}' \\ \mathbf{n}_w = \mathbf{R}\mathbf{n}' \end{cases} \tag{18}$$

The error vector $\mathbf{e}_{error}$ is obtained by subtracting the reference result $\mathbf{n}_{wc}$ from the calculated result $\mathbf{n}_w$:

$$\mathbf{e}_{error} = \mathbf{n}_{wc} - \mathbf{n}_w = (E_x, E_y, E_z)^T \tag{19}$$

where E_x, E_y, and E_z represent the X-axis, Y-axis, and Z-axis components of the error vector $\mathbf{e}_{error}$, respectively. $\mathbf{e}_{error}$ represents the spatial deviation between the error-containing vector rotated by the matrix obtained from the alignment operation and the error-free vector rotated by the reference matrix. According to Eq. (11), the vibration velocity vectors in the PCS are transformed via rotation matrices to the WCS and then superimposed to generate 3D vibrometry data.

To assess the overall system error, a normalized double integral of the 2-norm of the error vector $\mathbf{e}_{error}$ is performed over the domains of θ and σ:

$$E_{err} = \frac{\int_0^{\pi}\int_0^{\pi} \|\mathbf{e}_{error}\|_2 d\sigma d\theta}{\pi^2} \tag{20}$$

where the 2-norm represents the average spatial deviation between the error-containing vector rotated by the matrix obtained from the alignment operation and the error-free vector rotated by the reference matrix.. The normalized integration of this norm yields the relative distance error between algorithm-calculated alignment points and their actual counterparts.

In subsequent experiments, the quantity and distribution of calibration points for 3D alignment operation were varied, and the errors of rotation matrices obtained under different conditions were calculated based on the reference rotation matrices. This error evaluation methodology was employed to analyze the directional errors of the two rotation matrices at different scanning mirror rotation angles. Based on the experimental results, the optimal quantity and distribution of calibration points were determined.

3.3.1. *Calibration point number testing*

To verify the impact of calibration point quantity on the precision of the 3D alignment algorithm, systematic experimental analysis was conducted while maintaining consistent calibration region size and point distribution. 10 different calibration point quantities were established in the experiment, and the corresponding rotation matrices were calculated under each condition.

As the coordinate system of probe 1 serves as the WCS, only the errors of the calculated rotation matrices between probes 2, 3 and the WCS needed to be evaluated, with results illustrated in Fig. 9. In this analysis, F_{12} represents the error of the rotation matrix between probe 2 and the WCS calculated using Eq. (20), while F_{13} represents the error of the rotation matrix between probe 3 and the WCS. Fig. 9 demonstrates that the errors of the 3D alignment algorithm do not significantly decrease with increasing calibration point quantity, generally remaining within a 10 % when the calibration point quantity is 4~13.

3.3.2. *Calibration points distribution testing*

As demonstrated in the preceding discussion, increasing or decreasing the number of calibration points does not significantly affect the accuracy of the 3D alignment algorithm. Therefore, in this section, 6 calibration points were utilized to further examine the influence of calibration point distribution on algorithm accuracy under both uniform and concentrated distribution conditions. Fig. 10(a) and (b) illustrate the uniform and concentrated distributions of calibration points on the pipe, respectively. Experimental errors were calculated using Eq. (20), with the 2-norm of the error vector serving as the evaluation criterion. The experimental results are presented in Table 3. It can be seen that

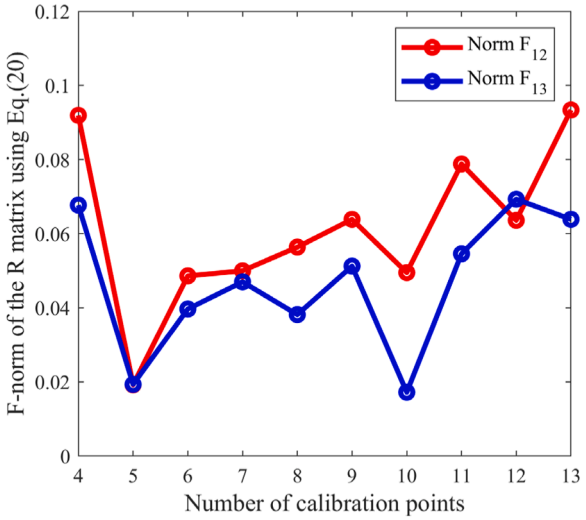

Fig. 9. Results of the number of 3D calibration points.

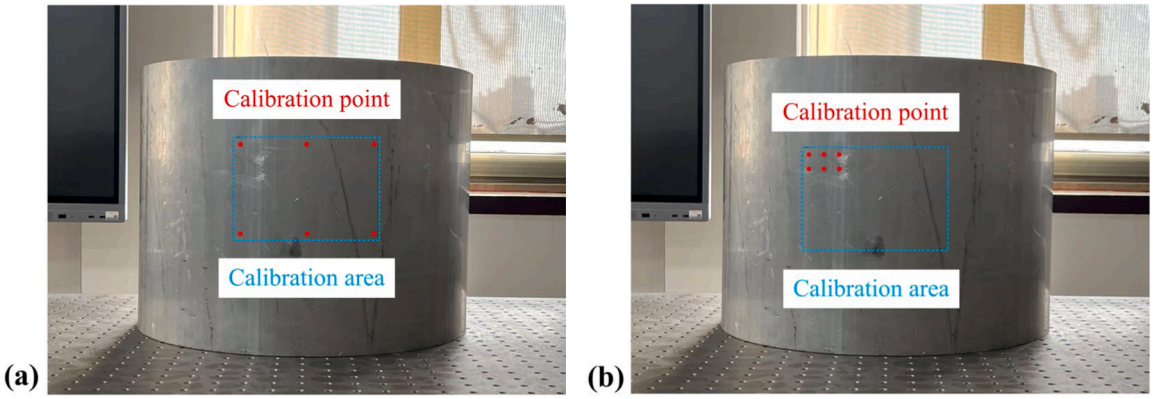

Fig. 10. Distribution of calibration points. (a) Uniformly distribution. (b) Dense distribution.

Table 3
Calibration points distribution testing results.

Probe No.	Error analysis for uniform distribution	Error analysis for concentrated distribution
2	5.0 %	10.2 %
3	4.7 %	24.0 %

uniformly distributed calibration points can improve precision to within 5 %. The results indicate that uniformly distributed calibration points yield smaller algorithm errors, whereas non-uniform, concentrated distributions lead to significantly increased errors. Therefore, in 3D alignment applications, calibration points should be distributed as uniformly as possible across the measured area to minimize algorithm errors.

3.3.3. *Summary*

In summary, after sufficient experimental exploration, the study has obtained the influence of key parameters on laser scanning control and 3D alignment accuracy. The results are summarized in Tables 4 and 5.

From Table 4, it can be concluded that the scanning control algorithm can achieve optimal performance when the fitting order is (2,2) and the number of calibration points exceeds 8.

Table 4
Scanning control error under different calibration parameters.

Influencing parameters	Values	RMSE(mm)	
		X-axis	Y-axis
Fitting order	(1,1)	0.34	1.15
	(1,2)	0.15	0.44
	(2,1)	0.21	0.63
	(2,2)	0.19	0.14
	(2,3)	0.38	0.58
	(3,2)	0.92	0.56
	(3,3)	2.75	1.92
	(3,4)	23.99	16.39
	(4,3)	18.66	28.41
	(4,4)	78.46	94.26
Number of calibration points	2	44.92	39.63
	3	44.07	38.65
	4	18.39	13.43
	5	2.64	3.03
	6	2.48	2.39
	7	0.31	1.05
	8	0.13	0.36
	9	0.18	0.28
	10	0.14	0.29
	11	0.16	0.26
	12	0.12	0.26
	13	0.13	0.38
Distribution of calibration points	Uniform	0.1	0.2
	Concentrated	7.6	43.9

Table 5
3D alignment error under different calibration parameters.

Influencing parameters	Values	Relative error	
		Probe 2	Probe 3
Number of calibration points	4	9.19 %	6.76 %
	5	1.92 %	1.93 %
	6	4.86 %	3.96 %
	7	4.99 %	4.70 %
	8	5.63 %	3.81 %
	9	6.38 %	5.12 %
	10	4.95 %	1.72 %
	11	7.88 %	5.45 %
	12	6.35 %	6.92 %
	13	9.33 %	6.38 %
Distribution of calibration points	Uniform	5 %	4.7 %
	Concentrated	10.2 %	24 %

From Table 5, it can be concluded that the number of calibration points does not affect the accuracy of the 3D alignment algorithm. To achieve the optimal performance of the algorithm, it is necessary to ensure that the calibration points are evenly distributed within the calibration area of the image captured by the camera.

4. Accuracy testing of 3D alignment

Section 3 provides a comprehensive analysis of various parametric factors affecting the accuracy and stability of scanning control and 3D alignment methods, including polynomial fitting order, calibration point quantity, and calibration point distribution. Section IV presents a research evaluation of 3D alignment accuracy based on the optimal algorithm parameters identified from the aforementioned test results, assessing the precision of the proposed 3D alignment algorithm.

In this section, the experimental methodology is identical to that described in Section III. In the experiment, the coefficient matrices $\boldsymbol{A}$ and $\boldsymbol{B}$ of the laser control algorithm were obtained from Section III. Subsequently, the laser was controlled to scan six uniformly distributed points to solve for the rotation matrices. The solved rotation matrices and the measured reference rotation matrices were substituted into Eqs. (18)-(19) to calculate the errors. The results are illustrated in Fig. 11, where (a) displays the errors along the X, Y, and Z axes for rotation matrix $\mathbf{R}_{12}$ between the PCS 2 and the global WCS, while (b) shows the corresponding errors for rotation matrix $\mathbf{R}_{13}$ between the PCS 3 and the global WCS.

Statistical analysis was conducted on the error components in Fig. 11 when the rotation matrix is applied to an arbitrary unit vector $\mathbf{n}' = (\sin\theta\cos\sigma, \sin\theta\sin\sigma, \cos\theta)$ with θ and σ varying from 0 to π. The X, Y and Z error components of the probe 2 range from-4.09 % to 6.15 %, −5.14

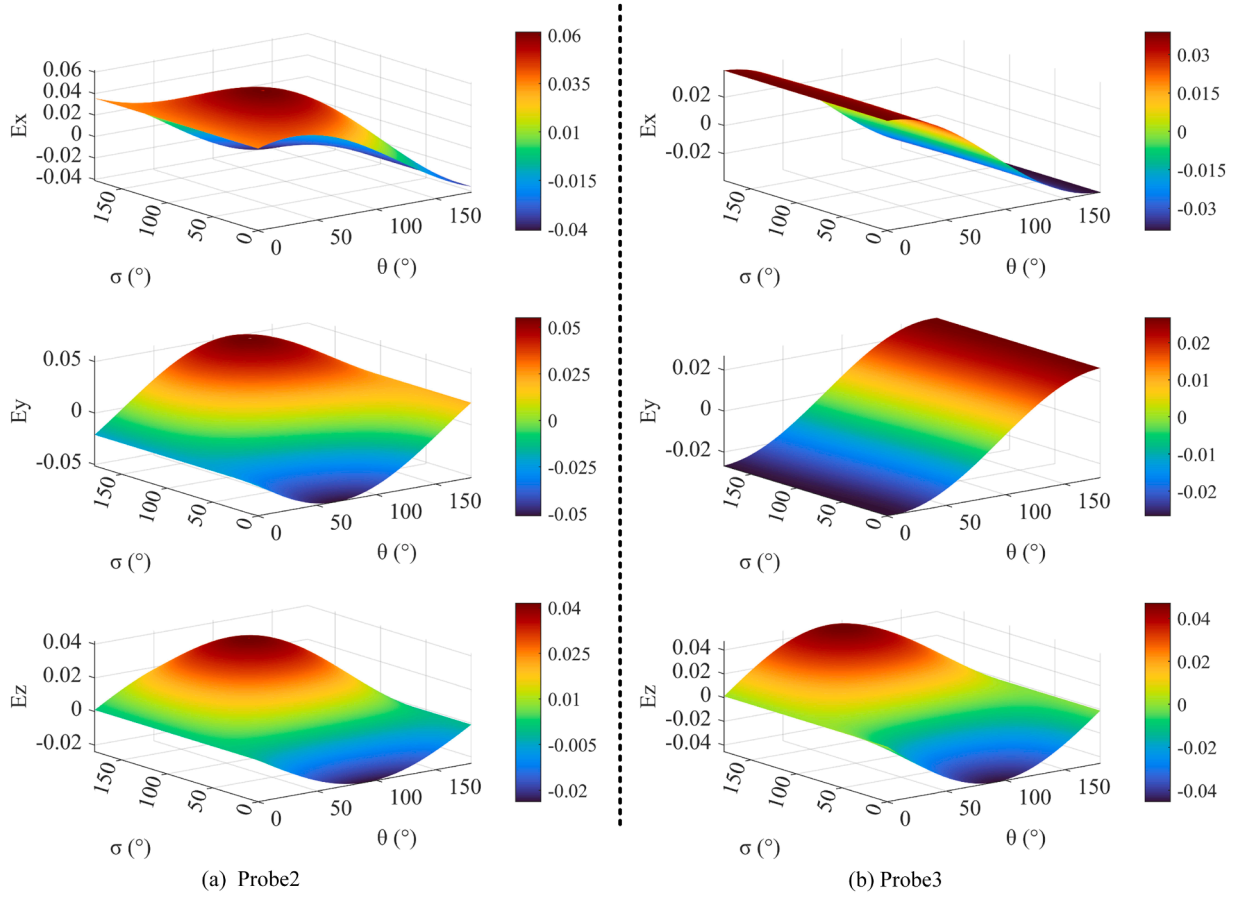

Fig. 11. 3D alignment error of pipe surface via applying the rotation matrix to an arbitrary unit vector $\mathbf{n}' = (\sin\theta\cos\sigma, \sin\theta\sin\sigma, \cos\theta)$. (a) X, Y, Z error component of the probe 2; (b) X, Y, Z error component of the probe 3.

% to 5.51 %, −2.38 % to 4.15 %, respectively, with average absolute errors of 3.15 %, 2.56 % and 1.67 %, root mean square errors of 3.55 %, 2.96 % and 2.06 %, respectively, and maximum errors of 6.15 %, 5.51 % and 4.15 %. The X, Y and Z error components of the probe 3 range from-3.88 % to 3.88 %, −2.67 % to 2.67 %, −4.53 % to 4.71 %, respectively, with mean absolute errors of 2.49 %, 1.71 % and 1.90 %, root mean square errors of 2.76 %, 1.90 % and 2.35 %, respectively, and maximum errors of 3.88 %, 2.67 % and 4.71 %. Furthermore, when the parameters θ and σ vary from 0 to π, as shown in Eq. (20), a 2-norm is used to represent the distance between the alignment point calculated by the algorithm and the actual alignment point. The normalized integration of this norm yields the relative distance error calculated by the algorithm between the alignment point and its actual counterpart. The 2-norm error was 4.27 % for the probe 2 and 4.71 % for the probe 3. The analysis shows that the errors of the probes 2 and 3 along all three axes remain essentially stable within the maximum range of 4.71 %.

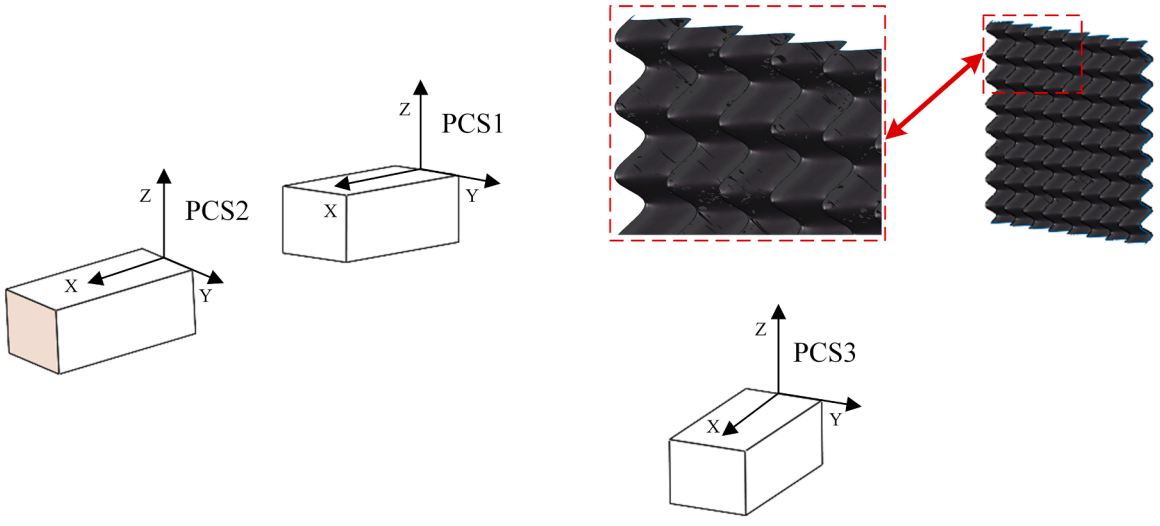

Fig. 12. Complex wavy surface's simulation model.

To validate the applicability of the proposed method to more complex surfaces, a wavy surface was selected as a representative case for investigation. Due to the challenges associated with physically manufacturing such a wavy surface, this study was conducted using SolidWorks simulations. A 3D model, as shown in Fig. 12, was created in SolidWorks.

The evaluation method uses the "Coordinate System" function under "Reference Geometry" to establish three probe coordinate systems within the 3D model, enabling the acquisition of the 3D coordinates of any point on the measured object in these different coordinate systems. To closely mimic real experimental conditions, random errors were introduced into the simulation for parameters such as angles and distances. The angular error was set with a range of $\pm 0.006^{\circ}$ and the distance error was ± 1 mm; they are consistent with the actual performance of the physical components used in the experiments. The results obtained under the condition of uniformly distributed calibration points are presented in Fig. 13.

A statistical analysis was performed on the error components shown in Fig. 13. The X, Y and Z error components of the probe 2 range from -2.56 % to 2.34 %, −2.09 % to 2.09 %, −2.73 % to 2.49 %, respectively, with average absolute errors of 1.54 %, 1.26 % and 1.12 %, with root mean square errors of 1.71 %, 1.40 % and 1.37 %, and with maximum errors of 2.56 %, 2.09 % and 2.73 %. The X, Y and Z error components of the probe 3 range from −3.13 % to 1.90 %, −3.00 % to 2.91 %, −2.15 % to 1.26 %, respectively, with mean absolute errors of 1.61 %, 1.55 % and 0.87 %, with root mean square errors of 1.82 %, 1.74 % and 1.07 %, and with maximum errors of 3.13 %, 3.00 % and 2.15 %. Furthermore, when the parameters θ and σ vary from 0 to π, as shown in Eq. (20), a 2-norm is used to represent the distance between the alignment point calculated by the algorithm and the actual alignment point. The normalized integration of this norm yields the relative distance error calculated by the algorithm between the alignment point and its actual counterpart. The 2-norm error was 2.52 % for the probe 2 and 2.64 % for the probe 3. The analysis result shows that the errors of the probes 2 and 3 along all three axes remain essentially stable within the maximum range of 2.64 %. This result demonstrates that the proposed method can also be effectively applied to complex surfaces.

5. Conclusion

(1) A generalized geometric model for 2D rotating mirrors was established to mathematically describe the relationship between mirror rotation angles and spatial vectors of emitted laser beams. The model enables precise estimation of the incident laser spot position, and subsequently achieves changes in spot position by adjusting the rotation angles of the scanning mirrors. This model is a key prerequisite for implementing three-dimensional scanning control and three-dimensional alignment operations.
(2) A laser orientation control algorithm was proposed to establish coordinate transformation relationships through polynomial fitting to achieve automatic scanning and precise control of laser incidence spots. Research demonstrates that optimal control precision is achieved with fitting order (2, 2), and errors are maintained within 0.2 mm; accuracy is maximized with 8–9 calibration points, and the errors are within 0.4 mm; uniformly distributed calibration points in pipe conditions enable precision within 0.2 mm. This method combines the advantages of high accuracy and computational simplicity.
(3) A 3D alignment algorithm based on singular value decomposition was developed to achieve precise alignment of three laser probes in 3D FFS LDV by determining coordinate transformation matrices. The

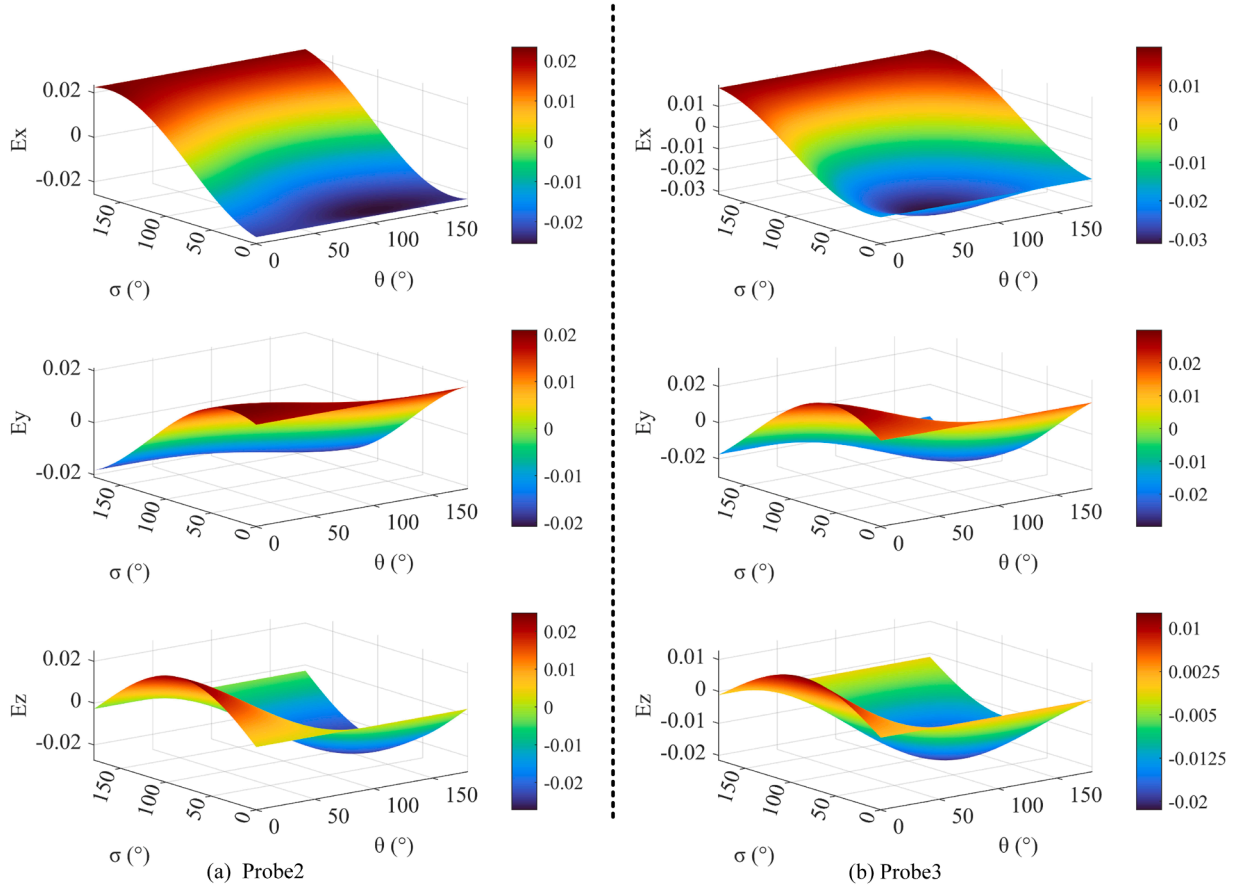

Fig. 13. 3D alignment error of complex wavy surface via applying the rotation matrix to an arbitrary unit vector $\mathbf{n}' = (\sin\theta\cos\sigma, \sin\theta\sin\sigma, \cos\theta)$. (a) X, Y, Z error component of the probe 2; (b) X, Y, Z error component of the probe 3.

measured laser-direction velocities from each probe were transformed into 3D vibration components in the global coordinate system using the derived rotation matrices. This capability is particularly crucial for applications like ultrasonic testing, where accurately measuring the full-field, out-of-plane and in-plane components of ultrasonic wave propagation is essential for defect detection and material characterization. Experimental validation confirms that calibration point quantity has minimal impact on accuracy, and errors are consistently maintained within 10 %; uniformly distributed calibration points can improve precision to within 5 %; pipe case testing demonstrates achievable accuracy of 4.71 %.

Although this study has achieved promising results with the 3D alignment system for 3D LDV, the system's performance depends on several environmental and target factors. The system requires adequate lighting conditions to ensure optimal laser spot detection and camera-based tracking accuracy. Additionally, it depends on the surface reflectivity of the target object, requiring a diffusely reflective surface with moderate reflectivity. The system cannot reliably measure surfaces that are either rough surfaces (causing excessive speckle noise) or highly specular surfaces (leading to beam deflection and signal loss). Moreover, the system may encounter challenges when measuring structures with extreme surface curvature, as significant curvature can distort the laser spot shape and intensity distribution, thereby complicating the centroid extraction process and consequently degrading both control and alignment accuracy. Furthermore, due to mirror rotation limitation, the current system cannot detect large-scale targets. Future research could involve integrating the system with a robotic arm, which would enable comprehensive testing of large-scale, complex structures through programmed arm movements.

In summary, this paper proposes a novel method for laser control and 3D alignment in 3D LDV. Compared to conventional approaches, this method achieves superior precision while eliminating the reliance on calibration boards. It provides a more efficient and streamlined approach for future development of high-precision 3D LDV.

CRediT authorship contribution statement

Zhengzhe Li: Writing – review & editing, Visualization, Software, Formal analysis, Data curation. **Zhipeng Zhang:** Writing – original draft, Software, Methodology, Data curation. **Ruqiang Lai:** Writing – review & editing, Investigation, Data curation. **Tao Zhang:** Visualization, Validation, Supervision. **Jian Li:** Methodology, Conceptualization. **Jinyu Ma:** Supervision, Software, Resources. **Xinjing Huang:** Writing – review & editing, Supervision, Project administration, Investigation, Funding acquisition, Conceptualization.

Declaration of competing interest

The authors declare the following financial interests/personal relationships which may be considered as potential competing interests:

Xinjing Huang reports financial support was provided by National Natural Science Foundation of China. Xinjing Huang reports financial support was provided by Natural Science Foundation of Tianjin. Xinjing Huang reports financial support was provided by Tianjin National Key Laboratory Major Project. Xinjing Huang reports financial support was provided by Guangxi Key Laboratory of Automatic Detecting Technology and Instruments. If there are other authors, they declare that they have no known competing financial interests or personal relationships that could have appeared to influence the work reported in this paper.

Acknowledgement

This work is supported by National Natural Science Foundation of China (No. 62473279), Natural Science Foundation of Tianjin (No. 24JCZDJC01070), Tianjin National Key Laboratory Major Project (24ZXZSSS00290) and Guangxi Key Laboratory of Automatic Detecting Technology and Instruments (No. YQ24203).

Data availability

Data will be made available on request.

References

[1] Yu T, Tang Q, Vinayaka S. Identifying structural properties of a steel railway bridge for structural health monitoring using laser doppler vibrometry. Autom Constr 2024;(160):105320.
[2] Yuan K, Zhu Z, Chen W, Zhu W. Development and validation of a new type of displacement-based miniatured laser vibrometers. Sensors 2024;24(16):5230.
[3] Delo G, Roy R, Worden K, Surace C. Using the inverse finite-element method to harmonise classical modal analysis with fibre-optic strain data for robust population-based structural health monitoring. Strain 2025;16(1):e12481.
[4] Ke W, Li L, He L, Yang P, Niu F, Han K, Fan R, Zhang H, Feng X. Accelerating the phase demodulation process based on a parallel hilbert transform with overlapping computation for a laser heterodyne doppler vibrometer. Opt Lett 2025;50(2):507–10.
[5] Hasheminejad N, Vuye C, Margaritis A, Van den bergh W, Dirckx J, Vanlanduit S. Characterizing the complex modulus of asphalt concrete using a scanning laser doppler vibrometer. Materials 2019;12(21):3542.
[6] Elhady A, Abdel-Rahman EM. Characterization of shear horizontal waves using a 1D laser doppler vibrometer. Sensors 2021;21(7):2467.
[7] Nie X, Zhou J. Pitch independent vehicle-based laser doppler velocimeter. Opt Lasers Eng 2020;(131):106072.
[8] Wu S, Wang D, Xiang R, Zhou J, Ma Y, Gui H, Liu J, Wang H, Lu L, Yu B. All-Fiber configuration laser self-mixing doppler velocimeter based on distributed feedback Fiber laser. Sensors 2016;16(8):1179.
[9] Kim D, Song H, Khalil H, Lee J, Wang S, Park K. 3-D vibration measurement using a single laser scanning vibrometer by moving to three different locations. IEEE Trans Instrum Meas 2014;63(8):2028–33.
[10] Kim D, Park K. Development of a three-dimensional vibration measurement system using a single laser scanning vibrometer and laser scanner. In: 13th IEEE International Conference Control Automation (ICCAS 2013); 2013. p. 1378–80.
[11] Margerit P, Gobin T, Lebée A, Caron J. The robotized laser doppler vibrometer: on the use of an industrial robot arm to perform 3D full-field velocity measurements. Opt Lasers Eng 2021;137:106363.
[12] Sels S, Vanlanduit S, Bogaerts B, Penne R. Three-dimensional full-field vibration measurements using a handheld single-point laser doppler vibrometer. Mech Syst Signal Process 2019;126:427–738.
[13] Rembe C, Kowarsch R, Ochs W, Dräbenstedt A, Giesen M, Winter M. Optical three-dimensional vibrometer microscope with picometer-resolution in x, y, and z. Opt Eng 2014;53(3):034018.
[14] Miyashita T, Fujino Y. Development of 3D vibration measurement system using laser doppler vibrometers. In: Proc. SPIE 6177, Health Monitoring and Smart Nondestructive Evaluation of Structural and Biological Systems V; 2006, 61770I.
[15] Chen D, Zhu W. Investigation of three-dimensional vibration measurement by a single scanning laser doppler vibrometer. J Sound Vib 2017;387(20):36–52.
[16] Yuan K, Zhu W. Estimation of modal parameters of a beam under random excitation using a novel 3D continuously scanning laser doppler vibrometer system and an extended demodulation method. Mech Syst Signal Process 2021;155:107606.
[17] Yuan K, Zhu W. In-plane operating deflection shape measurement of an aluminum plate using a three-dimensional continuously scanning laser doppler vibrometer system. Exp Mech 2022;62:667–76.
[18] Yuan K, Zhu W. A novel general-purpose three-dimensional continuously scanning laser doppler vibrometer system for full-field vibration measurement of a structure with a curved surface. J Sound Vib 2022;540(8):117274.
[19] Yuan K, Zhu W. Identification of modal parameters of a model turbine blade with a curved surface under random excitation with a three-dimensional continuously scanning laser doppler vibrometer system. Measurement 2023;214(15):112759.
[20] Zeng X, Wicks AL, Mitchell LD. Geometrical method for the determination of the position and orientation of a scanning laser doppler vibrometer. Opt Lasers Eng 1996;25(4–5):247–64.
[21] Martarelli M, Revel GM, Santolini C. Automated modal analysis by scanning laser vibrometry: problems and uncertainties associated with the scanning system calibration. Mech Syst Signal Process 2001;15(3):581–601.
[22] Xu Y, Miles RN. An identification algorithm for directing the measurement point of scanning laser vibrometers. Opt Lasers Eng 1995;22(2):105–20.
[23] Huang X, Chen S, Guo S, Xu T, Q M, Jin S. A 3D localization approach for subsea pipelines using a spherical detector. IEEE Sens J 2017;17(6):1828–36.
[24] Arun KS, Huang TS, Blosteinm SD. Least-squares fitting of two 3-D point sets. IEEE Trans Pattern Anal Mach Intell 1987;PAMI-9(5):698–700.
[25] Sorkine-Hornung O, Rabinovich M. Least-squares rigid motion using SVD. Computing 2017;1(1):1–5.